Ionization and radiation dynamics of carbon ablation plasmas

J. Ward Thornhill,[a] James J. Duderstadt, and Dwight P. Duston[b]
Department of Nuclear Engineering, University of Michigan, Ann Arbor, Michigan 48109

(Received 3 December 1986; accepted for publication 14 April 1987)

A computational model that can be used for studying the ablation physics of medium z targets by ion beams is presented. In particular, the interaction of a proton beam as it heats and ablates a carbon target is analyzed. Because the radiation emitted during the interaction can carry away a significant amount of the total target energy, the radiation and ionization dynamics is treated carefully. This is accomplished by incorporating a collisional-radiative equilibrium model into the ionization dynamics package of a one-dimensional hydrodynamics model. Cold target energy deposition is assumed, thus eliminating the need for resolving the energy deposition after each time step. The errors incurred by this assumption are discussed. The computer simulation is applied to a general parameter study that involves varying the initial beam conditions to see effects upon the evolution of the target. In addition, the amount of $K\alpha$ radiation produced by the direct interaction of the beam particles with the individual target atoms is calculated. This information is useful for diagnostic purposes since it is highly dependent upon the ionization state of the target.

I. INTRODUCTION

The theoretical modeling of the interaction of an energetic charged particle beam with matter is useful for a variety of applications including inertial confinement fusion (ICF), x-ray production, and ion beam implantation. One of the earlier beam target models developed to study this problem was that of Peleg and Zinamon[1] in which they modeled the ablation of gold and copper targets by a proton beam. They also treated radiative losses in their model. In order to include finite temperature effects, Mehlhorn[2] developed an ion deposition model that is very useful for ICF targets. It is capable of handling the stopping of an arbitrary ion traversing a material of arbitrary composition, density, and temperature. More recently, Rogerson[3] has treated the deposition of a proton beam in an aluminum target whereby the hydrodynamics and radiation dynamics is treated in a fully self-consistent manner.

The principal objective of this work is to provide a simple framework in which to study the physical processes which take place during the ablation of a target resulting from a particle beam interaction. In particular, a proton beam impacting upon a carbon target is analyzed. This is accomplished by coupling a one-dimensional, single-temperature fluid hydrodynamic code to an ionization dynamics and an energy deposition model. Because the radiation emitted during the evolution of the ablation plasma has a significant effect on the energetics and also because it provides useful diagnostic information, the ionization dynamics have been modeled very carefully. To do this, a collisional-radiative equilibrium (CRE) model[4,5] which includes a large number of excited states and atomic processes, is employed.

The computer simulation is applied to several studies and applications. The effect of initial beam conditions on plasma parameters is examined. As anticipated it is found that both the energy of the particles which comprises the beam and the power density of the beam have a large influence on the evolution of the plasma and its radiation field. This is manifested in a number of plasma parameters, including the energy partitioning among internal, kinetic, potential, and radiative components. In addition we have examined the amount of $K\alpha$ radiation[6] that is produced by the direct interaction of the beam particles with the individual target atoms.

II. IONIZATION DYNAMICS MODEL

Because the problems considered here span a large range of temperatures and density values, we need an ionization dynamics model which is comprehensive enough to accommodate lower-density plasmas, where radiative effects become significant in determining the ion populations, as well as to account for the transitions to higher-density local thermodynamic equilibrium (LTE) conditions. For this reason we chose a collisional-radiative equilibrium (CRE) model.

The atomic states that provide the basis for the model are the ground state and typically 6–12 of the lowest excited levels of each ion specie (see Table I). In some cases the included levels are representative of a combination of nearby degenerate states. For example, most levels of carbon IV (3 times ionized), V, and VI are modeled according to principal quantum number n, that is, the properties of the various nl sublevels have been averaged over angular momentum and magnetic quantum numbers.

Although the number of states included must be limited, the model should be adequate for modeling the relevant physics of the simulations. This is because the reduced ionization potentials for densities in excess of 10^{20} cm^{-3} impose a cutoff at an effective quantum number n' that is near or within the range of the included states. The free-electron densities encountered in our problems are almost always

[a] Naval Research Laboratory, Washington, DC 20375.
[b] Strategic Defense Initiative Organization, Pentagon 20301-7100.

 0021-8979/87/161181-08$02.40

TABLE I. Atomic data for carbon (CRE) model.

Carbon states	Energy (eV)	Stat. weight	Configuration	Carbon states	Energy (eV)	Stat. weight	Configuration
C I(1)	0.000	9	$1s^2 2s^2 2p^2 : 3p$ ground	C III(4)	17.05	9	$1s^2 2p^2 : 3p$
C I(2)	1.264	5	$1s^2 2s^2 2p^2 : 1d$	C III(5)	18.09	5	$1s^2 2p^2 : 1d$
C I(3)	2.684	1	$1s^2 2s^2 2p^2 : {}^1s$	C III(6)	22.63	1	$1s^2 2p^2 : 1s$
C I(4)	4.183	5	$1s^2 2s 2p^3 : {}^5s$	C III(7)	32.61	27	$1s^2 2s 3s : {}^3p$
C I(5)	7.485	9	$1s^2 2s^2 2p 3s : {}^3p$				$3p : {}^3s, {}^3p, {}^3d$
C I(6)	7.685	3	$1s^2 2s^2 2p 3s : {}^1p$				$3d : {}^3p, {}^3d, {}^3f$
C I(7)	7.946	15	$1s^2 2s 2p^3 : {}^3d$	C III(8)	33.15	9	$1s^2 2s 3s : {}^1p$
C I(8)	8.727	27	$1s^2 2s^2 2p 3p : {}^3s, {}^3p, {}^3d$	C III(8)	33.15	9	$1s^2 2s 3p : {}^1s, {}^1p, {}^1d$
C I(9)	8.866	9	$1s^2 2s^2 2p 3p : {}^1s, {}^1p, {}^1d$				$3d : {}^1p, {}^1d, {}^1f$
C I(10)	9.330	9	$1s^2 2s 2p^3 : {}^3p$	C III(9)	39.71	48	$1s^2 2p 4s : {}^3p$
C I(11)	9.706	15	$1s^2 2s^2 2p 3d : {}^1p, {}^1d, {}^1f$				$4p : {}^3s, {}^3p, {}^3d$
C I(12)	9.729	45	$1s^2 2s^2 2p 3d : {}^3p, {}^3d, {}^3f$				$4d : {}^3p, {}^3d, {}^3f$
C II(1)	0.000	6	$1s^2 2s^2 2p : {}^2p$ ground				$4f : {}^3d, {}^3f, {}^3g$
C II(2)	5.536	12	$1s^2 2s 2p^2 : {}^4p$	C III(10)	39.98	16	$1s^2 2p 4s : {}^1p$
C II(3)	9.290	10	$1s^2 2s 2p^2 : {}^2d$				$4p : {}^1s, {}^1p, {}^1d$
C II(4)	11.96	2	$1s^2 2s 2p^2 : {}^2s$				$4d : {}^1p, {}^1d, {}^1f$
C II(5)	13.72	6	$1s^2 2s 2p^2 : {}^2p$				$4f : {}^1d, {}^1f, {}^1g$
C II(6)	17.08	18	$1s^2 2s^2 3s : {}^2s$	C III(11)	40.87	81	$1s^2 2p 3s : 3p$
			$3p : {}^2p$				$3p : {}^3s, {}^3p, {}^3d$
			$3d : {}^2d$				$3d : {}^3p, {}^3d, {}^3f$
C II(7)	17.61	4	$1s^2 2p^3 : {}^4s$	C III(12)	41.30	27	$1s^2 2p 3s : {}^1p$
C II(8)	18.66	10	$1s^2 2p^3 : {}^2d$				$3p : {}^1s, {}^1p, {}^1d$
C II(9)	20.68	32	$1s^2 2s^2 4s : {}^2s$				$3d : {}^1p, {}^1d, {}^1f$
			$4p : {}^2p$	C IV(1)	0.000	2	$1s^2 2s : {}^2s$ ground
			$4d : {}^2d$	C IV(2)	8.010	6	$1s^2 2p : {}^2p$
			$4f : {}^2f$	C IV(3)	37.55	2	$1s^2 3s : {}^2s$
C II(10)	20.92	6	$1s^2 2p^3 : {}^2p$	C IV(4)	39.68	6	$1s^2 3p : 2p$
C III(1)	0.000	1	$1s^2 2s^2 : {}^1s$ ground	C IV(5)	40.28	10	$1s^2 3d : {}^2d$
C III(2)	6.499	9	$1s^2 2s 2p : {}^3p$	C IV(6)	50.80	32	$n = 4$:doublet
C III(3)	12.69	3	$1s^2 2s 2p : {}^1p$	C IV(7)	55.78	50	$n = 5$:doublet
C V(1)	0.000	1	$1s^2 : {}^1s$ ground				
C V(2)	299.0	3	$1s 2s : {}^3s$				
C V(3)	304.3	1	$1s 2s : {}^1s$				
C V(4)	304.4	9	$1s 2p : {}^3p$				
C V(5)	307.9	1	$1s 2p : 1p$				
C V(6)	353.5	27	$n = 3$:triplet				
C V(7)	354.5	9	$n = 3$:singlet				
C V(8)	370.7	64	$n = 4$:s and t				
C V(9)	378.5	100	$n = 5$:s and t				
C VI(1)	0.000	2	$1s : {}^2s$ ground				
C VI(2)	367.5	8	$n = 2$:doublet				
C VI(3)	435.6	18	$n = 3$:doublet				
C VI(4)	459.4	32	$n = 4$:doublet				
C VI(5)	470.4	50	$n = 5$:doublet				
C VII	000.0	1	bare nucleus				

larger than this, except possibly for the cold compressed regions of the target.

The atomic processes which are represented are collisional ionization, three-body recombination, collisional excitation, collisional deexcitation, spontaneous emission, radiative recombination, and dielectronic recombination. They are shown schematically along with their corresponding transitions in Fig. 1.

The atomic processes are manifested in a set of rate equations, one for each atomic state, having the form

$$\frac{dN_i}{dt} = \sum_j C_{ji} N_j - \sum_j C_{ij} N_i ,$$

where N_i is the population density of atomic level i and C_{ji} is the sum of the reaction rates representing the atomic processes for transitions from state j to i. The rate coefficients, C_{ij}'s, were obtained from the Naval Research Laboratory. The processes and methods used to calculate them have been previously documented by Duston *et al.*[7]

With the exception of possibly the hot tenuous ablation region, the hydrodynamic time scales which are typically of the order 10^{-9}–10^{-11} s are long in comparison to the relaxation times of the atomic states. Thus we are reasonably justified in assuming that the equilibrium nature of the CRE model is valid for our problems, i.e., we can set the left-hand side of the above equation equal to zero.

Once the equations are solved for the population densities it is a straightforward calculation to find the effective charge, specific heats, ionization energy, radiation field, and other information that depends upon knowledge of the populations.

We have included radiative cooling due to line, recom-

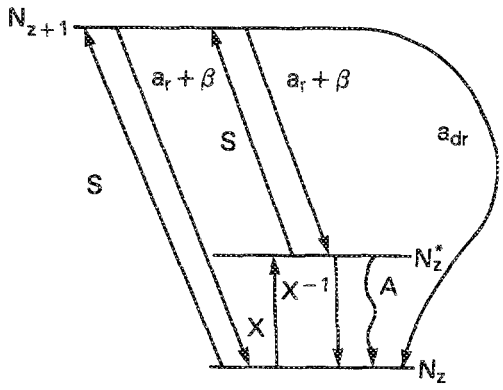

FIG. 1. Three-level diagram displaying the atomic processes represented in the model. S is collisional ionization, a_r is radiative and three-body recombination, a_{dr} is dielectronic recombination, X is electron collisional excitation, X^{-1} is collisional deexcitation, and A is spontaneous emission.

bination, and bremsstrahlung radiation for the simulations described in this paper; however, since no transport of radiation is performed, the model is only strictly valid for optically thin plasmas. It should also be mentioned that we have neglected the explicit effect of reduced ionization potentials on the rate coefficients. This approximation could have an impact upon the high-density results.

III. HYDRODYNAMIC MODEL

The effective charge, specific heats, and radiation cooling rates calculated in the above section are then incorporated into a hydrodynamics model. The model developed for these studies is based upon the WAZER and FIRE codes of Kidder[8] and McCarville,[9] respectively. These codes utilize a Lagrangian one-dimensional, single fluid model. Similar to FIRE, we assume a single temperature for the ions and electrons. This is a valid assumption for the plasma conditions of interest, because the electron-ion equilibration time t_{eq} is shorter than the hydrodynamic time scales.

Briefly, the set of equations solved in this model are conservation of mass, momentum, and energy, and an equation of state, written in Lagrangian form:

Conservation of mass

$$\dot{v} = v(\nabla \cdot \tilde{u}) ;$$

conservation of momentum

$$\dot{\tilde{u}} = -v\nabla(p+q) ;$$

conservation of energy

$$C_v \dot{T} = -T\left(\frac{\partial p}{\partial T}\right)_v \dot{v} + v\nabla\cdot(\kappa\nabla T) + s - q\dot{v} ;$$

equation of state

$$pv = kT/m \quad \text{(ideal gas law)} ,$$

where v is the specific volume, $\tilde{u}$ is fluid velocity, p is pressure, q is an artificial viscosity, T is temperature, m is the atomic mass, κ is thermal conductivity, C_v is specific heat, and s is a combination of the radiative loss and particle beam deposition source terms.

IV. ENERGY DEPOSITION MODEL

The hydrodynamics model is set up to include the deposition due to a proton beam that has both a fixed current density and initial particle energy up to 10 MeV. The stopping power formulas used are those of Ziegler and Andersen.[10] They represent a proton being stopped in a cold carbon target. Because temperature effects are not considered, the amount of energy deposited in each zone per unit time will remain constant for a square wave beam pulse. This eliminates the need for resolving the energy deposition after each time step.

The energy deposited in each hydrodynamic zone is calculated using

$$E_i = I\int_x^{x+\Delta x_i} \frac{\partial E}{\partial x}\, dx ,$$

where E_i is the energy deposited per unit time in zone i, Δx is the zone width, I is the beam current density (assumed constant until the beam is completely stopped), and $\partial E/\partial x$ is the stopping power. It may appear that the assumption that temperature effects are negligible is not very good; however, we find that for these simulations the errors incurred are about 30% for "worst case" situations, i.e., temperature and density regimes encountered that are likely to violate the cold temperature assumption. Although substantial, this error is acceptible in light of the level of detail we are trying to retain. To illustrate, Fig. 2 shows a plot of the stopping power for the cold target in juxtaposition to several graphs of "worst case" situations where temperature effects have been considered. The formula used for temperature dependent "worse case" calculations are the Bethe formula[11] for bound-electron and Jackson's formula[12] for free-electron stopping powers.

For a more comprehensive treatment of the effects of temperature dependence, see the paper by Rogerson.[3]

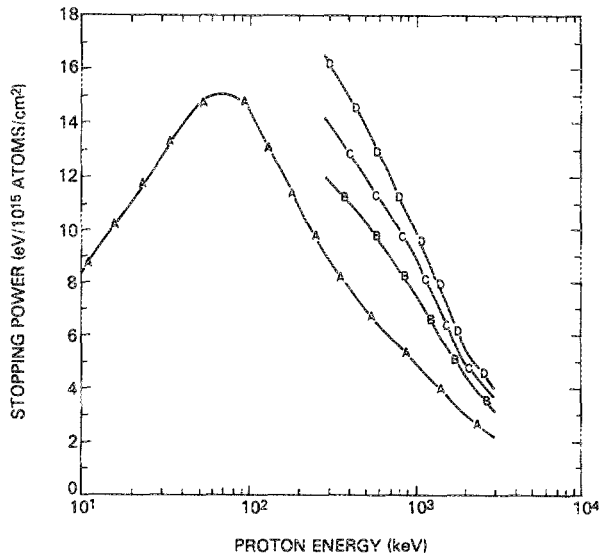

FIG. 2. Stopping powers for protons in carbon. Curve A represents the Ziegler and Andersen cold target stopping powers. B, C, and D represent temperature-dependent values for an electron temperature of 50 eV, an effective charge of 4, and ion densities of 10^{22}, 10^{21}, and 10^{20} cm^{-3}, respectively.

V. $K\alpha$ PRODUCTION

Aside from examining the general evolution of the target, we are also interested in looking at $K\alpha$ production due to the direct interaction of the beam with the target atoms. Therefore, before going into the details of the simulations, we want to discuss the calculation of $K\alpha$ emission.

$K\alpha$ emission is produced by the interaction of fast particles or photons with a target atom in which a vacancy in the K shell is produced. When the subsequent vacancy is filled by a decaying outer orbital electron, the excess energy will be used either to ionize another outer shell electron in a process known as an Auger transition or else a photon will be emitted. The relative occurrence of these possibilities is quantified by the fluorescence yield, the fraction of all K-hole creations in which the excited atom emits a characteristic $K\alpha$ photon in its deexcitation.

In this investigation the interest is upon knowing how much $K\alpha$ radiation is produced by the direct interaction of the beam with the target atoms. This information can be used as a diagnostic tool for checking upon the amount of beam energy that is incident upon the target; it also provides knowledge of the ionization state of the plasma. Competing with the beam in producing $K\alpha$'s will be that produced by thermal agitation of the plasma and inner-shell photoionization. The first of these is not a concern for this investigation because thermal energies are relatively low and do not attain values comparable with the binding energies of the K-shell electrons. However, there will be situations in which a significant percentage of the radiation field will be in the energy range which exceeds the threshold value for K-shell photoionization. When this happens, because of the larger cross section for inner-shell photoionization,[13] $\simeq 10^{-18}$–10^{-20} cm^2 for frequencies of interest, compared to impact ionization by the beam, $\simeq 10^{-21}$ cm^2, the beam $K\alpha$ calculation is not very meaningful. Still, it can be used for times up to those in which the high-energy radiation field becomes a consideration. Note, that when the $K\alpha$'s produced by inner-shell photoionization are present the photon flux producing the vacancies is usually several orders of magnitude larger than the beam flux. Thus, the rate of K-shell vacancy production via inner-shell photoionization might be 5–6 orders of magnitude greater than that produced by the beam.

The calculation is performed by scaling the experimental values of Khan, Potter, and Whorley[14] for $K\alpha$ production by proton bombardment of neutral carbon to the C II, C III, and C IV ionization stages. To accomplish this, the binary encounter approximation (BEA)[15] is used. It states that the cross section for creating a K-shell vacancy by particle bombardment scales as $1/U^2$, where U is the binding energy of the K-shell electron. Since the cross section for $K\alpha$ emission can be found from this vacancy production cross section by multiplying by ω, the fluorescence yield, it is a straightforward procedure to calculate the $K\alpha$ emission cross sections for the other ion stages, provided the fluorescence yields are known, using

$$\sigma_i = \sigma_1 \, (\omega_i/\omega_1) \, (U_1/U_i)^2 ,$$

where σ_i is the cross section for $K\alpha$ emission by ion stage $i[i = 1,2,3,4$ correspond to C I (neutral carbon) C II, C III, and C IV]. Values for binding energies U_i's and fluorescence yields ω_i's are listed in Table II.

TABLE II. Fluorescence yields and binding energies. N_i is the total ion number density (cm^{-3}).

	C I	C II	C III	C IV
Charge	0	1	2	3
K shell Binding energy (eV)	284	302	329	359
ω_K	0.014	0.014	0.030	$[24 + N_i(2.3\times10^{-20})]^{-1}$

The conditions of validity for the BEA approximation are given by

$$Z_1/Z_2 \ll 1 \quad \text{and} \quad Z_1/Z_2 \ll v/v_e ,$$

where Z_1 is the atomic number of the projectile, Z_2 is the atomic number of the target atom, v is the velocity of the projectile, and v_e is the K-shell electron velocity. For our problems of interest, the above inequalities will be satisfied so long as the projectile energy exceeds about 0.6 MeV.

The values for fluorescence yield for the C I, C II, C III, and C IV ion stages, listed in Table II, are taken from several sources and in some cases they had to be estimated. The C I value of 0.014 is obtained from Khan, Potter, and Whorley. Since information on C II was unavailable, we chose the same value as used for C I. The basis for this assumption is that the fluorescence yields of C I- and C II-like ionization stages of aluminum are about the same.[6] The fluorescence yield for the C III ionization stage is found by a statistical weighting of the ratio of the dielectronic recombination rates[16] to the total decay rate for the $1s2s^2$ and $1s2s2p$ states of lithiumlike C IV. Likewise, the fluorescence yield for C IV had to be calculated. Since the removal of an inner-shell electron from C IV leaves the system in a singly excited state of C V, the fluorescence yield in this case is calculated by a statistically weighted average of the ratio of line emission of the total decay rate.

Having knowledge of cross sections, binding energies, and the fluorescence yields it is possible to calculate the $K\alpha$ radiated power per unit mass. It is found for each target zone by the following formula:

$$\frac{\text{Power}}{\text{unit mass}} = \frac{IA}{N_{\text{tot}}} \sum_{i=1}^{4} \sigma_i \, U_i \, N_i ,$$

where A is the number of carbon atoms per unit mass, I is the current density, N_{tot} is the total ion density, and N_i is the ion density of ion stage i.

VI. APPLICATIONS AND RESULTS OF NUMERICAL SIMULATIONS

In this section we discuss the numerical results for (a) a typical simulation run which displays the evolution of the target and radiation field during the beam-target interaction and (b) a parameter study in which beam energy and current density are varied to determine their effect upon essential plasma parameters, such as internal energy, radiation conversion efficiencies, and $K\alpha$ production.

A. Typical simulation run

This simulation is for a proton beam striking a 100-μm-thick foil of soild carbon of density 2.2 g/cm^3 that is surrounded by a vacuum. The power density is 10^{12} W/cm^2 and the initial energy of the protons is 2 MeV. The beam is shaped as a 10-ns square-wave pulse.

The spatial and temporal evolution of the target density is illustrated in Fig. 3 where curves A, B, C, D, and E correspond to snapshots in time of 0, 1.2, 3.1, 6.0, and 8.1 ns. Because the projected range of a 2-MeV proton in a cold carbon target is $\simeq 40\,\mu$m, the beam will deposit its energy in the outer third of the target and, since there are no temperature effects taken into consideration, the amount of energy deposited in each zone remains constant throughout the duration of the pulse. From Fig. 3 we see that the demarcation of the energy deposition region is where each of the curves crosses curve A on the right-hand side. We see that the material to the left of the deposition region becomes quickly compressed to about five times solid-state density while the density in the region to the right-hand side decreases to about one tenth solid-state density by the end of the pulse. The compression is due to shocks created by the large ablation pressures, $\simeq 10^4$ J/cm^3, produced in the deposition region. The crest of the mass density curve travels at the sound speed of the target which is $\simeq 7\times 10^5$ cm/s for densities of 11 g/cm^2 and temperatures near 10 eV. One notices the peculiar behavior whereby the density curves precipitously fall at the end of the deposition region, level off, and then begin to rise in the blowoff region, the reason being that there is more energy deposited at the end of the range of the protons as they slow down in the carbon (see Fig. 2). This, in turn, creates a higher ablation pressure area near the deposition–cold target interface which not only compresses the cold part of the target but also material further to the right. As expected, we find that the density in the deposition region drops off substantially as the region ablates.

Figure 4 shows the temperature evolution of the target

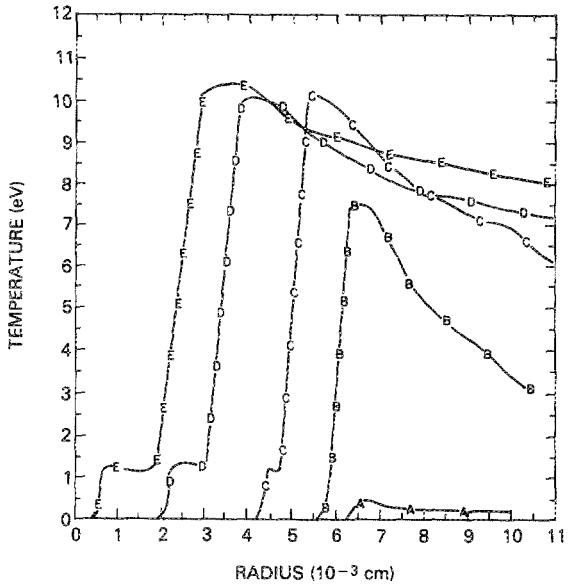

FIG. 4. Temperature as a function of time and position for a particle beam of 2 MeV protons at an intensity of 10^{12} W/cm^2 ablating a 100-μm-thick carbon target. A, B, C, D, and E represent 0.0, 1.2, 3.1, 6.0, and 8.1 ns, respectively.

for the same times depicted in Fig. 3. We find that temperatures rapidly rise to 10 eV and then saturate at this value in a time of 3 ns. The nondeposition region remains cold, less that 2 eV, throughout the interaction. Shock heating, compressional work, and thermal conduction are the primary heating mechanisms in this region. If radiation transport had been included, we might see that absorption of inner-shell radiation[16] also contributes to heating the cold part of the target. The peak in the temperature curves correspond to the regions where the maximum deposition is occurring in the target and, as for the pressure curves shown in Fig. 3, this is near the end of the range of the proton beam.

Figure 5 illustrates how the energy is partitioned during

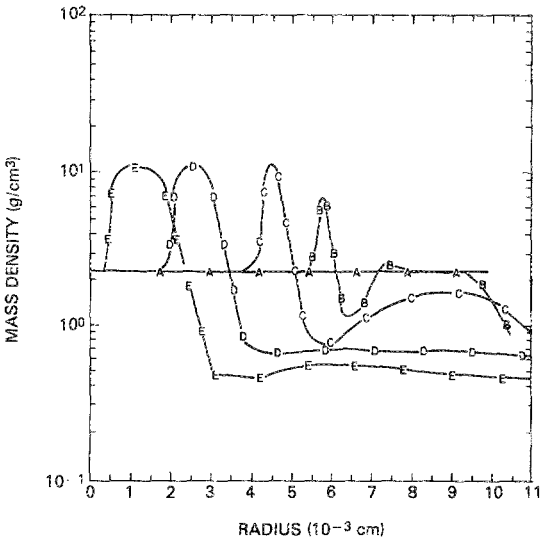

FIG. 3. Mass density as a function of time and position for a particle beam of 2 MeV protons at an intensity of 10^{12} W/cm^2 ablating a 100-μm-thick carbon target. A, B, C, D, and E represent 0.0, 1.2, 3.1, 6.0, and 8.1 ns, respectively.

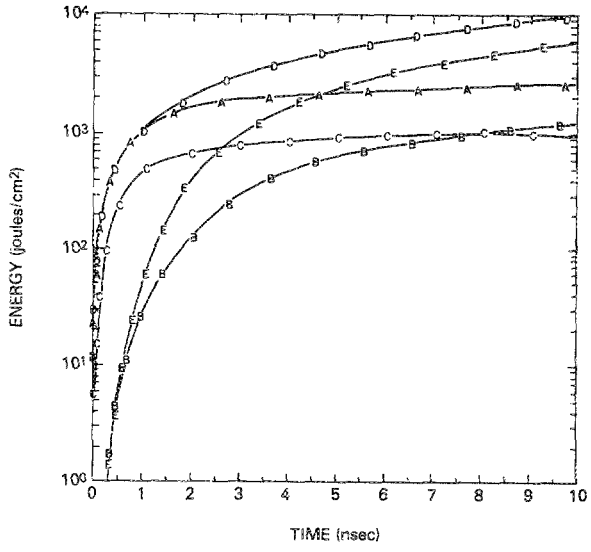

FIG. 5. Energy partitioning as a function of time for a beam of 2 MeV protons at an intensity of 10^{12} W/cm^2 ablating a 100-μm-thick carbon target. A is internal, B is kinetic, C is ionization, D is the total source, and E is the total radiative energy.

target evolution. We find that about 50% of the beam energy is radiated away by the end of the beam pulse. This is an overestimation, because there would be some reabsorption of the radiation field, a process not yet accounted for in this model. During the first 3 ns we see that most of the beam energy is going into internal energy of the deposition region. Since the ionization energy is small compared to the total internal energy, most of this energy is thermal energy of the ions and electrons. The temperature and density conditions are such that the ionization and internal energies have nearly saturated after 4 ns, and any additional source energy is either immediately radiated away or else contributes to the kinetic energy of the target.

The $K\alpha$ energy is shown in Fig. 6 and as expected the $K\alpha$ emission originating from C I and C II dominates because of the relatively cool temperatures encountered in this problem. This is readily seen in Fig. 7 where the ion abundance curves for a typical ion density, 5×10^{22} cm^{-3}, are displayed. An examination of this figure along with Fig. 4 show that we should expect to see a large contribution of $K\alpha$ coming from C I throughout the pulse but only copious amounts of C II and C III $K\alpha$'s as the temperature rises during the later part of the interaction. Because the $K\alpha$ lines have appreciably different energies they should be spectrally discernable. The line energies are 284, 302, 329, and 359 eV for the parent atom being in a C I, C II, C III, or C IV state, respectively.

B. Parameter study

Tables III, IV, and V contain information about beam, internal, kinetic, radiative, and ionization energies for 10-ns square-wave beam pulses of 10^{12}, 10^{13}, and 10^{14} W/cm^2 ablating a 100-μm-thick planar target. Each table is then divided into three sections corresponding to an initial proton beam energy of 1, 2, and 3 MeV. The data represent a cross section of the target parameters taken at a time $t = 9$ ns.

We see that the radiation conversion efficiency varies from 54% for a power density of 10^{12} W/cm^2 and proton energy of 3 MeV, up to 91% for a power density of 10^{14} W/cm^2 and proton energy of 2 MeV. It appears that the trend is for conversion efficiencies to increase with power density, but it does not seem that they are as affected by changes in initial proton energy. This is because there is corresponding-

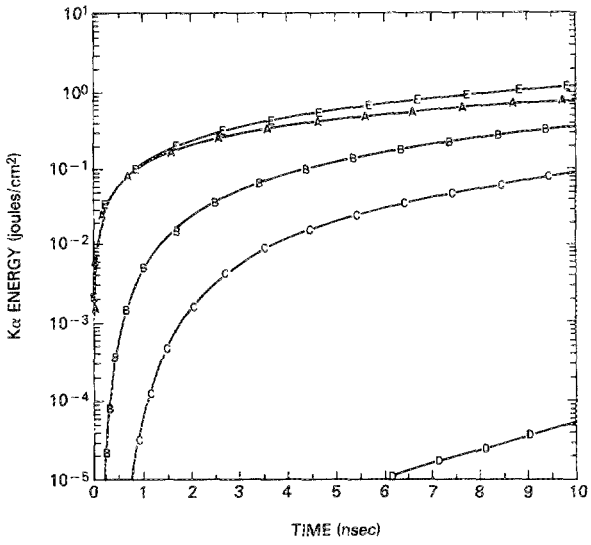

FIG. 6. $K\alpha$ energy spectrum as a function of time during the ablation of a 100-μm-thick carbon target by a beam consisting of 2 MeV protons at an intensity of 10^{12} W/cm^2. Curve A represents $K\alpha$'s of 284 eV; B—302 eV; C—329 eV; D—359 eV; and E represents the total $K\alpha$ energy emitted.

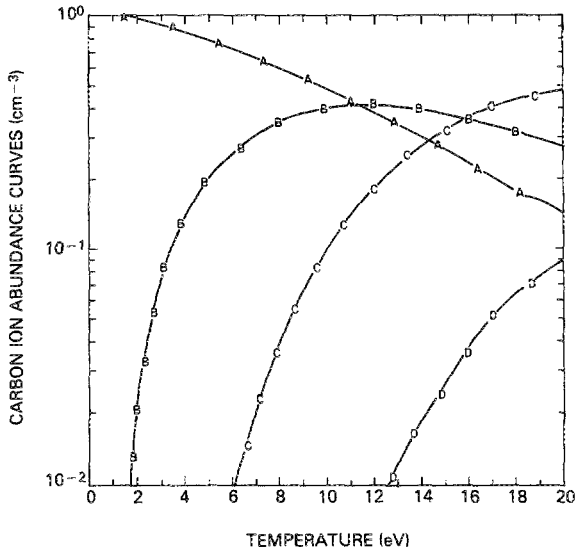

FIG. 7. Carbon ion abundance curves as a function of temperature for a total ion density of 5×10^{22} cm^{-3}. Curve A, B, C, and D correspond to C I, C II, C III, and C IV, respectively.

TABLE III. Parameter study for a beam of power density 10^{12} W/cm^2. Energies in units of (10^3 J/cm^2) and percentage of total beam energy are listed.

Plasma energy parameters	Initial ion energy (1 MeV)	Initial ion energy (2 MeV)	Initial ion energy (3 MeV)
Beam	9.0 (100%)	9.0 (100%)	9.0 (100%)
Internal	1.9 (21%)	2.7 (30%)	3.2 (36%)
Kinetic	1.2 (13%)	1.1 (12%)	0.95 (11%)
Radiative	5.9 (65%)	5.2 (58%)	4.9 (54%)
Ionization	0.87 (10%)	1.0 (11%)	1.3 (14%)
Line	3.0 (32%)	2.4 (27%)	2.4 (27%)
Free-bound	1.8 (20%)	1.4 (15%)	1.2 (14%)
Free-free	1.2 (13%)	1.4 (15%)	1.3 (14%)
Line energies (% of radiative energy)			
$E<10$ eV	3%	7%	13%
$10<E<20$ eV	15%	26%	28%
$20<E<60$ eV	31%	13%	8%
$60<E<100$ eV	0%	0%	0%
$100<E<200$ eV	0%	0%	0%
$200<E<350$ eV	0%	0%	0%
$E>350$ eV	0%	0%	0%
Free-bound energies (% of radiative energy)			
$E<10$ eV	0%	1%	5%
$10<E<20$ eV	17%	15%	13%
$20<E<60$ eV	13%	9%	6%
$60<E<100$ eV	0%	0%	0%
$100<E<200$ eV	0%	0%	0%
$200<E<350$ eV	0%	0%	0%
$E>350$ eV	0%	0%	0%

TABLE IV. Parameter study for a beam of power density 10^{13} W/cm^2. Energies in units of (10^4 J/cm^2) and percentage of total beam energy are listed.

Plasma energy parameters	Initial ion energy (1 MeV)	Initial ion energy (2 MeV)	Initial ion energy (3 MeV)
Beam	9.0 (100%)	9.0 (100%)	9.0 (100%)
Internal	1.0 (11%)	0.95 (11%)	1.1 (12%)
Kinetic	0.86 (10%)	0.67 (7%)	0.66 (7%)
Radiative	7.2 (80%)	7.4 (82%)	7.1 (78%)
Ionization	0.35 (4%)	0.43 (5%)	0.46 (5%)
Line	2.1 (23%)	2.3 (26%)	2.2 (24%)
Free-bound	3.9 (43%)	2.8 (31%)	2.3 (25%)
Free-free	1.3 (14%)	2.3 (26%)	2.7 (30%)
Line energies (% of radiative energy)			
$E<10$ eV	1%	2%	2%
$10<E<20$ eV	1%	4%	7%
$20<E<60$ eV	15%	21%	8%
$60<E<100$ eV	0%	0%	0%
$100<E<200$ eV	0%	0%	0%
$200<E<350$ eV	8%	0%	0%
$E>350$ eV	4%	0%	0%
Free-bound energies (% of radiative energy)			
$E<10$ eV	0%	0%	0%
$10<E<20$ eV	0%	1%	7%
$20<E<60$ eV	24%	31%	23%
$60<E<100$ eV	20%	5%	2%
$100<E<200$ eV	8%	0%	0%
$200<E<350$ eV	0%	0%	0%
$E>350$ eV	1%	0%	0%

TABLE V. Parameter study for a beam of power density 10^{14} W/cm^2. Energies in units of (10^5 J/cm^2) and percentage of total beam energy are listed.

Plasma energy parameters	Initial ion energy (1 MeV)	Initial ion energy (2 MeV)	Initial ion energy (3 MeV)
Beam	9.0 (100%)	9.0 (100%)	9.0 (100%)
Internal	0.89 (10%)	0.45 (5%)	0.52 (6%)
Kinetic	0.49 (5%)	0.47 (5%)	0.45 (5%)
Radiative	7.7 (85%)	8.2 (91%)	8.1 (90%)
Ionization	0.22 (2%)	0.17 (2%)	0.18 (2%)
Line	2.3 (25%)	2.6 (29%)	1.5 (17%)
Free-bound	4.8 (53%)	4.1 (45%)	3.9 (43%)
Free-free	0.6 (7%)	1.5 (17%)	2.6 (29%)
Line energies (% of radiative energy)			
$E<10$ eV	0%	0%	0%
$10<E<20$ eV	0%	0%	0%
$20<E<60$ eV	2%	6%	11%
$60<E<100$ eV	0%	0%	0%
$100<E<200$ eV	0%	0%	0%
$200<E<350$ eV	8%	14%	4%
$E>350$ eV	14%	11%	3%
Free-bound energies (% of radiative energy)			
$E<10$ eV	0%	0%	0%
$10<E<20$ eV	0%	0%	0%
$20<E<60$ eV	0%	4%	20%
$60<E<100$ eV	8%	20%	19%
$100<E<200$ eV	19%	18%	8%
$200<E<350$ eV	5%	0%	0%
$E>350$ eV	30%	7%	1%

ly less mass in the deposition region for the beam that has the smaller initial proton energy. There is an obvious difference in the size of the deposition region for the different proton energies because the ranges for a 1, 2, and 3 MeV proton in cold solid carbon are 10, 40, and 70 μm, respectively. Another observation is that the radiation spectrum is harder for the smaller proton energies. Again, this is due to the beam being absorbed by correspondingly less mass of the target. Thus, the region heats up faster and reaches higher temperatures, as high as 50 eV for power densities of 10^{14} W/cm^2, than those heated by beams of identical power density but comprised of more energetic protons.

If opacity effects had been included, one would expect to see slightly higher ionization and internal energies, a harder radiation spectrum, and a net radiation loss less than the results quoted in this study.

The total beam-produced $K\alpha$ energy emitted by the target up to time $t = 9$ ns is given in Table VI. An interesting feature of this table is that the $K\alpha$ energies scale with beam intensity for the 3 MeV protons, however, we find that this scaling is not valid for the other proton energies. Once again this is due to the larger mass that is included in the deposition region for the higher-energy protons. For the 3 MeV case, there is sufficient mass to absorb the beam such that temperatures remain low enough that only C I, C II, C III, and C IV states exist. This is not true for the lower initial proton energy beams which can quickly burn through these levels if the intensity is large enough. This is substantiated by Table V where we see that the radiation spectrum is so hard, for the low initial proton energy case, that most of it must have eminated from the K shell.

By measuring the energy of the $K\alpha$ radiation field from the beginning of the interaction, an experimentalist could use a table such as this to discern the beam power density or particle energies. Also, since the frequency of the $K\alpha$ photon depends upon the ionization state of the parent atom, one can obtain knowledge of the ionization state of the deposition region by comparing experimental $K\alpha$ spectra to computational predictions. Note that because of the presence of a radiation spectrum whose frequency exceeds the binding energy of the inner-shell electrons and can therefore create additional K-shell vacancies, the $K\alpha$ results are only meaningful for the lower-power densities. Even though the beam-produced $K\alpha$ spectrum has rather limited utility for carbon, it could be a worthwhile diagnostic for higher-z elements at the larger power densities.

VII. CONCLUSION

We have developed a computational model which simulates the ablation of a carbon target by a proton beam. This is

TABLE VI. $K\alpha$ energies (J/cm^2).

Power density (W/cm^2)	Initial ion energy (1 MeV)	Initial ion energy (2 MeV)	Initial ion energy (3 MeV)
10^{12}	0.84	1.0	1.3
10^{13}	4.9	13.0	15.0
10^{14}	7.0	37.0	99.0

done by coupling a sophisticated CRE ionization dynamics model, a one-dimensional, single fluid and temperature hydrodynamics model, and a simple temperature-independent energy deposition model. The total package is then applied to simulating the beam-target interaction under a variety of initial beam conditions.

An examination of the results of our parameter study shows that radiation conversion efficiencies can be as high as 90% for optically thin targets. We also find that the thermal emission profile is strongly dependent upon both the energy and power density of the beam. This is illustrated by the observation that the hardness of the radiation field can be increased by either using less energetic protons and maintaining the same power density or else increasing the power density. The parameter study also categorizes the dependence of internal, kinetic, and radiative energy upon beam power density and proton energy.

Another application investigated was the calculation of the amount of $K\alpha$ photon energy emitted due to the beam protons knocking out inner-shell electrons. We found that under optically thin conditions, the energy density of this emission is several orders of magnitude below that of the thermally produced radiation field. However, since the energy of the $K\alpha$'s is larger than the other photons, it should be easily resolvable. It was also noted that the beam produced $K\alpha$ results are only valid when the target is relatively cold. Otherwise, there will be a significant component of high-energy photons created by valence transitions that will also be absorbed by the K shell and produce their own $K\alpha$ emission, thus swamping the beam-produced $K\alpha$ results. Because the spectrum of $K\alpha$ depends upon the binding energy of the K-shell electron of the emitting atom, it represents of measure of the ionization state of the target.

ACKNOWLEDGMENTS

While J. Thornhill was at The University of Michigan this work was supported by AFSOR Grant No. 80-0029. Afterwards, it was supported by the NRC and ONR. The authors would also like to thank G. A. Moses and T. A. Mehlhorn for their contributions.

[1]E. Peleg and Z. Zinamon, Phys. Fluids **24**, 1528 (1981).
[2]T. Mehlhorn, J. Appl. Phys. **52**, 6522 (1981).
[3]J. E. Rogerson, R. W. Clark, and J. Davis, Phys. Rev. A **31**, 3323 (1984).
[4]R. W. P. McWhirter, *Plasma Diagnostic Techniques* (Academic, New York, 1968).
[5]D. Bates, A. Kingston, and R. McWhirter, Proc. R. Soc. London Ser. A **267**, 297 (1962).
[6]E. Nardi and Z. Zinamon, J. Appl. Phys. **52**, 7075 (1981).
[7]D. Duston, R. W. Clark, J. Davis, and J. P. Apruzese, Phys. Rev. A **27**, 1441 (1983).
[8]R. Kidder and W. Barnes, University of California Radiation Laboratory Report No. UCRL-50583 (1971).
[9]T. McCarville, R. Peterson, and G. Moses, Comput. Phys. Commun. **28**, 367 (1983).
[10]H. Andersen and J. Ziegler, *Hydrogen Stopping Powers and Ranges in All Elements* (Pergammon, New York, 1977).
[11]H. Bethe, Ann. Phys. **5**, 325 (1930).
[12]J. D. Jackson, *Classical Electrodynamics* (Wiley, New York, 1975).
[13]F. Biggs and R. Lighthill, Sandia Laboratories Report No. SC-RR-71 0507 (Reprint 1982).
[14]J. Khan, D. Potter, and R. Whorley, Phys. Rev. **139**, A 1735 (1965).
[15]D. Madison and E. Merzbacher, *Atomic Inner-Shell Processes* (Academic, New York, 1975).
[16]D. Duston, J. E. Rogerson, J. Davis, and M. Blaha, Phys. Rev. A **28**, 2968 (1983).